A Dataset for Radar Scattering Characteristics of Vehicles Under Real-World Driving Conditions: Major Findings for Sensor Simulation

Lukas Elster, Martin F. Holder, and Manuel Rapp

***Abstract*—In the virtual validation of automated driving, trustworthy simulation models of perception sensors are required. Radar sensors are particularly hard to model, as their measurements are notoriously difficult to interpret. This is due to their complex measurement principle, involving multipath propagation of mm-waves, varying backscattering characteristics of objects, and further factors such as limited measurement ranges and resolutions that introduce uncertainty to the measurements. This work presents a method for studying the backscatter characteristics of vehicles under real-world driving conditions. A slalom-like driving scenario, which is representative of road driving where the vehicle is visible under different aspect angles, has been designed. It aims at a high level of reproducibility of the trajectories driven by the vehicles, hence reducing additional sources of uncertainty that were otherwise present in the measurements. In a large-scale measurement campaign, 13 vehicles have been studied. The vehicles under test are observed by multiple radars, mounted at different heights, and carry reference sensors for obtaining their positions. In this article, we present the measurement campaign and show major findings from our measurement results. Our focus lies on drawing conclusions for trustworthy sensor simulation. Both sensor measurement data and MATLAB code for data analysis are made publicly available alongside this article.**

***Index Terms*— Millimeter-wave sensors, sensor model analysis, sensor testing and evaluation.**

I. Introduction

VIRTUAL test methods are required for the release of automated driving. Such methods use simulation models of the involved sensor modalities. Radar sensors are of the utmost importance for automated driving functions, due to their ability to measure relative velocity, robustness against adversarial weather conditions, and low costs in comparison to frequency-modulated continuous-wave (FMCW) lidar systems.

Still, the development of simulation models of radar sensors, which are ready for deployment in simulation-based testing toolchains, is the subject of current research. A research problem, that is closely linked to radar sensor simulation, is the ability to model mm-wave scattering behavior realistically in virtual environments. Radar measurements are known to have a noisy characteristic, which originates from the measurement principle. Physically interpretable quantities, such as range, velocity due to the Doppler effect, and angular positions are deduced from spectral analysis of modulated mm-wave signals.

The backscattered energy is dictating the existence and achievable accuracy of radar detection. In radar theory, the physics for obtaining backscatter is conceptually absorbed in the radar cross section (RCS) denoted as σ. It is a measure of the strength of the signal reflected by an object. Influencing factors include object size, geometry, material, wavelength, and aspect angle under which the object is visible to the

Manuscript received 20 October 2022; revised 13 January 2023; accepted 13 January 2023. Date of publication 24 January 2023; date of current version 28 February 2023. This work was supported in part by the German Federal Ministry for Education and Research (BMBF) through Virtual Validation Tool Chain for Automated and Connected Driving (VIVID) under Grant 16ME0173 and in part by the Open Access Publishing Fund of the Technical University of Darmstadt. The associate editor coordinating the review of this article and approving it for publication was Prof. Qiliang Li. *(Lukas Elster and Martin F. Holder contributed equally to this work.) (Corresponding author: Lukas Elster.)*

The authors are with the Institute of Automotive Engineering, Technical University of Darmstadt, 64287 Darmstadt, Germany (e-mail: lukas.elster@tu-darmstadt.de; martin.holder.tuda-alumnus@gmx.de; manuel.rapp@stud.tu-darmstadt.de).

Digital Object Identifier 10.1109/JSEN.2023.3238015

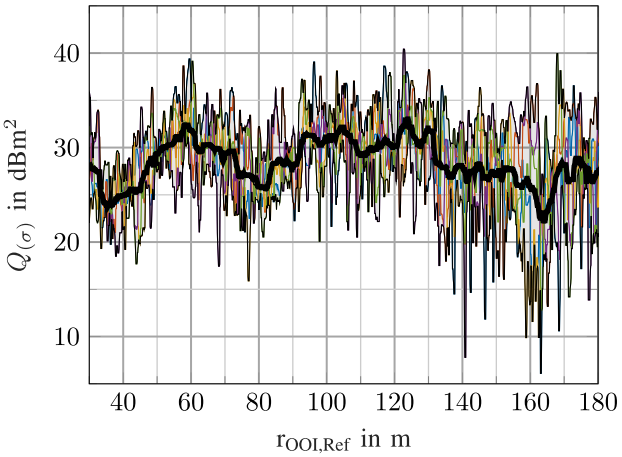

Fig. 1. Stochastic nature of RCS observed for a vehicle during five trials. The average value is indicated as a bold line and is obtained by using a moving average filter over 2.5 s. In our work, we use $Q_{(\sigma)}$ to denote RCS in the logarithmic scale, and σ for the linear scale.

sensor [1]. When inserted into the radar equation [2], as given in the following equation, the received power P_{Rx} can be obtained:

$$P_{\mathrm{Rx}} = P_{\mathrm{Tx}} \frac{G^2\, V_{\mathrm{mp}}^2\, \sigma\, \lambda^2}{(4\pi)^3\, r^4}. \tag{1}$$

Here, P_{Tx} denotes the transmitted power, and G, λ, and r denote the antenna gain, wavelength, and radial distance, respectively. This equation disregards the atmospheric attenuation and introduces V_{mp} as the so-called shaking factor ($0 \leq V_{\mathrm{mp}} \leq 2$) to account for influences by multipath propagation.

The RCS is well known, or analytically available, for simple geometries such as flat plates, spheres, or corner cube reflectors (CCRs). Analytical models are, however, not available for large objects with complex surfaces, such as vehicles.

In automotive radars, the RCS of objects is not measured directly. Instead, it is inferred from the received signal strength, the radial distance, and the angular position. Therefore, influences due to the free-space propagation loss, which is governed by r^{-4}, and the antenna gain pattern are compensated. Still, it is widely used as a quantification of the backscatter on an ordinal scale. Therefore, RCS, indicating the intensity of a detection, allows for object detection or free space estimation [3]. The noisy characteristic of the received power is also present when obtaining the corresponding RCS values in measurements. This is illustrated by the following example, obtained in a simple scenario where a vehicle is placed in front of the Ego vehicle, where "Ego" refers to the radar sensor carrier vehicle. As it is traveling at a higher speed than the Ego, the distance between the cars increases gradually. The RCS of the detections associated with the object of interest (OOI) are displayed in Fig. 1 and a distinct stochastic nature of the RCS is visible. By smoothing the noisy measurements, a moderately constant RCS value is revealed. This is, however, overlaid by additional phenomena, for example, multipath propagation, that causes a significant spread between repetitions and even adjacent measurement values. These results indicate that RCS measurement is influenced by the number of factors in a stochastic, nondeterministic fashion.

Radar models must be validated with real data to allow their usage for virtual safety validation. Therefore, the virtual environment is assessed together with the sensor model, as the real sensor is also subject to many real-world effects outside of idealized testbench conditions and anechoic radar chambers.

Although methods from the field of computational electromagnetic wave propagation allow us to compute backscatter profiles, it is debatable to what extent such simulation results may be transferred into real-world conditions. In reality, effects like multipath propagation and interference directly influence the RCS profiles and the validity of analytical models in comparison to real-world measurements, as it is highlighted in [4] and [5]. Similarly, measurement campaigns conducted in anechoic radar chambers need yet to prove their applicability to field measurements on public roads.

Therefore, we conducted an open-source available large-scale measurement campaign to obtain vehicle RCS patterns from automotive radar sensors under real driving conditions.

A. Related Work

The noisy and random nature of RCS is a well-known phenomenon in many radar applications. In radar literature, stochastic behavior is also referred to as fluctuation loss. Prominent research on this topic was carried out already in 1954 by Swerling [6]. He derived probabilistic models based on Rayleigh distributions describing the statistical properties of the RCS of objects with complexly formed surfaces, such as an aircraft. However, their application to automotive radar application, operating at mm-waves, is limited as different conditions apply here: Most notable is the presence of multipath reflections, for example, induced by reflections of the pavement, which are not present in airborne radar.

For automotive radar, a number of researchers have carried out reflectivity measurements in anechoic chambers obtained with automotive-grade radars, or vector network analyzers [7], [8]. Here, a vehicle has been placed on a rotating plate and its 360° RCS profile has been obtained from the received signal strength for a given rotation angle. Direct applicability of such results to automotive scenarios is not immediate, since the distance between radar and object is often chosen to be very small (e.g., less than 25 m), which is debatable for two reasons: First, the Fraunhofer criterion for far-field with typical aperture sizes in automotive radar is only fulfilled with 15 m onward. Second, long-range radar usually deploys high-pass filtering to avoid overloading the analog-to-digital (AD) converter for detections close to the sensor. Nevertheless, these results retain their validity and the fact that comparable results have been generated in different studies emphasizes their integrity. As the RCS profile is computationally expensive to calculate, simplified models have been derived. Based on observations and measurements, so-called "scattering center models" have been proposed [9], [10]. This theory assumes the total reflectivity of complex geometries such as vehicles is composed of individual scatterers. At the same time, there are areas on the vehicle from which a stronger backscatter is expected, such as the license plate, the wheel arches, or the exterior mirrors. The challenge with such models is the deduction of generalizability to different vehicle types and sizes, as large databases are missing.

In recent years, more radar datasets became publicly available, such as View-of-Delft [11], Radar Scenes [12], nuScenes [13], and others. They are designed for benchmarking and development of object detection and classification algorithms. It is difficult to extract reproducible scenarios for detailed RCS investigations from such datasets. In most scenes, parked (static) vehicles can be seen, or the rear of the vehicles in front while following behind. Annotations are often only available via lidar or bounding boxes, which typically do not have the precision of dedicated global navigation satellite system (GNSS) measurements.

We, therefore, design our study of vehicle backscatter such that it is representative of real road traffic conditions and at the same time generates a broad statement through many repetitions of the experiment and the use of different vehicles.

The measurement data,[1] and the evaluation source code[2] are all open-source and publicly available.

B. Research Questions and Method Outline

We state the following research questions, which we see as particularly relevant when studying the RCS characteristics in real-world traffic conditions, also in the light of radar simulation.

RQ1: What is the influence of the aspect angle of the radar to the object? Vehicles are often seen by the radar under different perspectives, for example, during lane changes. Our work addresses this research question by obtaining measurements of vehicles that follow a slalom-shaped trajectory. Therefore, they are visible under different aspect angles while conducting multiple repetitions to strengthen the underlying database for evaluation of the experiments. Utilizing a slalom course for studying reflectivity has been carried out in the author's previous work [14].

RQ2: What is the influence of the radar mounting height on RCS? In today's vehicles, radars are usually mounted at different heights. In order to study the effect of mounting height on the measured RCS, we use six identical radar sensors, mounted on a sensor rack (cf. Fig. 2).

RQ3: What is the influence of vehicle body shape on RCS? In everyday traffic, a wide variety of vehicles is encountered. Variations in their individual RCS profile are expected, due to differences in geometry, size, and material compounds. A total number of 13 vehicles of different categories (e.g., compact car, sedan, and truck) have been used in this study.

RQ4: Where is the strongest backscatter located depending on aspect angle and body shape? The position of radar detections with the highest RCS per measurement cycle is expected to depend on the aspect angle as well as the body shape of the vehicle. By comparing different vehicles scattering centers and scattering characteristics can be revealed.

II. Experimental Setup

The overall experimental setup and calibration methods for the measurement campaign as well as the quality criterion of the driven trajectory are explained in this chapter.

[1] https://www.fzd-datasets.de/rcs/

[2] https://gitlab.com/tuda-fzd/fzd-datasets/rcs-measurement

Fig. 2. Mounted sensor rack with six radar sensors at the front of the Ego vehicle. The rack has a lateral offset of 265 mm to the center. In addition to the radars and GNSS, it is also carrying lidar sensors. They are not considered in this work but the lidar data is also available within the published dataset.

TABLE I
MOUNTING HEIGHTS OF THE RADAR SENSORS

Sensor	Radar 1	Radar 2	Radar 3	Radar 4	Radar 5	Radar 6
h in mm	931	817	716	617	501	388

A. Sensors, Measurement Setup, and Calibration

Our research vehicle is a 2018 Mercedes-Benz S450 retrofitted with multiple Continental ARS408 radar sensors that are stacked on top of each other. Fig. 2 shows the installed measurement rack of the six radar sensors at the front of the vehicle. These radars are open-market adaptions of Continentals fourth-generation long-range radars, representing state-of-the-art automotive-grade 77-GHz radar [15]. This setup enables investigating the influence of the mounting height on the RCS profile of an OOI. The mounting heights of the sensors, measured from the ground to the center of the sensor, are specified in Table I. Due to the interference mitigation techniques of the manufacturer, interference is only recognizable in a raised signal to noise ratio (SNR) because of the six mounted sensors. As there are six same sensors used, we assume that the results focusing on RCS values are not affected based on our measurement setup.

These positions include above-average sensor heights for currently available vehicles, for example, the radar position in the Mercedes-Benz GLS series [16].

For obtaining the vehicle positions and motion, both the Ego vehicle and the OOI are equipped with the real-time kinematic (RTK)-based GNSS device automotive dynamic motion analyzer (ADMA).

Radar calibration was conducted both extrinsically and intrinsically. For extrinsics, CCRs have been placed at precisely measured positions with respect to the radar for obtaining the horizontal twist angles due to mounting. Intrinsic calibration aims at verifying the RCS value obtained by the radar. This is realized by placing a CCR with predefined RCS at a known distance from the radar (e.g., 40 m) over minimal-reflecting terrain. Both the radar and the CCR are mounted at a height of 3 m to avoid disturbances due to ground reflections.

Calibration of the relative positions between the Ego and OOI, both obtained with GNSS systems, is done by aligning

them along their rear axles, indicating zero longitudinal offsets. At standstill, the lateral offset can then be determined with a measurement tape. The known values for longitudinal and lateral offset are compared to the in the GNSS systems measured relative position data. These calibration values absorb uncertainties during obtaining mounting positions and are considered during the processing of the measurement data.

The radars report a set of detection points at a scan rate of approximately 14 Hz. Each scan contains a range, radial velocity by utilizing Doppler effect, azimuth, and RCS, and the radars are able to transmit up to 250 detections per measurement cycle. As large objects can cause multiple detections, the total RCS of an object is found by the linear sum over $n_{\mathrm{d,max}}$ detections that are linked to the object, that is,

$$Q_{(\sigma)} = 10 \log_{10} \sum_{k=1}^{n_{\mathrm{d,max}} \leq 250} \sigma_k. \tag{2}$$

The association of detections with an object is determined by multistage filtering that relies on the relative position and velocities of the OOI reported by the GNSS. The GNSS system samples at 100 Hz. While the GNSS system is reporting a precise time stamp, time referencing is made by time-stamping the individual data packages upon receiving via controller area network (CAN) bus. The radars are not synchronized in their measurement cycles. In other words, the measurement cycles of the radar sensors are independent of each other, that is, it cannot be guaranteed that the radar scans are performed simultaneously among all six radars.

B. Slalom Construction

The test setup consists of a sinusoidal slalom with ten periods. We briefly describe the setup of the slalom course, which is optimized for high repeatability for driving through it, and minimal effort for construction on straight roads. For each run, the OOI approaches the slalom setup driving straight ahead, with an offset to the center line. It is followed by the Ego vehicle which continues driving straight ahead on the center line while the OOI follows the sinusoidal trajectory of the slalom. The slalom parameters are designed to match distances and aspect angles that are similar to the real-world driving scenario of the OOI entering a curve, followed by the Ego vehicle when assuming a German EKL3-type road [17]. The geometry of the slalom is defined by the amplitude $\hat{y}$ and the frequency f_{Sla}. $\hat{y}$ is defined as 5 m to ensure a wide spectrum of aspect angles between Ego vehicle and OOI. The frequency is chosen as $f_{\mathrm{Sla}} = 0.014(1/\mathrm{m})$, which results in a slalom period of approximately 71 m. In test runs with an amplitude of 5 m, this frequency proved to be effortlessly manageable by the driver. The given geometric parameters result in a maximum yaw angle of ${}_{\mathrm{S}}\psi_{\mathrm{OOI}} = 25°$ referred to the slalom's center line. To define the relative movement between the Ego vehicle and the OOI, the corresponding speeds, v_{OOI} and v_{Ego}, as well as the initial distance between the two vehicles Δr are used. While driving through the slalom course, the OOI is visible to the Ego vehicle under different aspect angles: Its azimuth and yaw angles are changing periodically and both are opposed in phase, that is, maximum yaw is obtained at 0 azimuth, and vice versa. Fig. 3 illustrates the geometrical quantities.

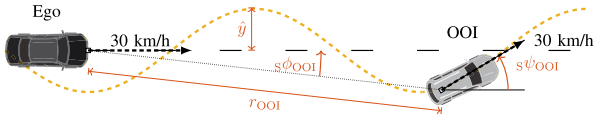

Fig. 3. Measurement setup of slalom with corresponding parameters where ${}_{\mathrm{S}}\phi_{\mathrm{OOI}}$ is denoted as the azimuth angle and r_{OOI} denoted as the range in the polar sensor coordinate system, ${}_{\mathrm{S}}\psi_{\mathrm{OOI}}$ is denoted as the yaw angle difference between the Ego vehicle and OOI as well as $\hat{y}$ is denoted as the slalom's amplitude.

The Ego vehicle's speed v_{Ego} is set to 30 km/h. This is the lowest possible speed that allows for the usage of speed control systems in both vehicles, although not all OOIs are equipped with equivalent systems. The target speed of the OOI v_{ooi} is also set to 30 km/h. By using the lowest speed possible, the duration of each experiment execution is maximized and therefore also the number of measurement samples. The sinusoidal trajectory and therefore a longer travel path in comparison to the Ego produce the most representative distance ranges with respect to the aspect angle. Lower speeds are preferred to generate as many data samples as possible during the slalom run. The usage of speed control systems causes a better reproducibility of the slalom runs, however, since they have to be manually set independent of each other, they also cause a deviation of the initial distance between Ego and OOI.

In order to guide the driver of the OOI along the ideal trajectory, traffic cones are placed along the slalom. For their placement, a sinusoidal function congruent to the ideal trajectory is calculated and eight equidistant sampling points per period are obtained. These sampling points include both vertices as well as both inflection points of each period. Each one of these characteristic positions is marked with two tall traffic cones which the OOI passes in between. The spacing between the two traffic cones is adjusted to and exceeds the width of the OOI. This is due to the fact that the reference point for the determination of the OOI's position is set as the center of the rear axle. Therefore, the front axle's center position can differ significantly from the ideal trajectory which requests additional space requirements. The four remaining sampling points are marked with flat cones over which the OOI passes. Fig. 4 shows the fully constructed slalom course. For each vehicle, ten slalom runs with five in each direction are conducted.

C. Evaluation of Trajectory

To evaluate the uniformity of the trajectory, a quality criterion based on the Hilbert transform is introduced. The Hilbert transform phase shifts a sinusoidal signal, in this case, either the trajectory of the OOI or $\hat{y}$ over x_{OOI}, by 90°. The result is an analytical signal $z(x_{\mathrm{OOI}})$, consisting of the initial signal as a real part and the phase-shifted signal as the imaginary part. This signal is referred to as $z(x)$ in the following paragraphs. To derive a quality criterion from this mathematical transformation, the absolute of the analytical signal is calculated. For an ideal trajectory, this would result

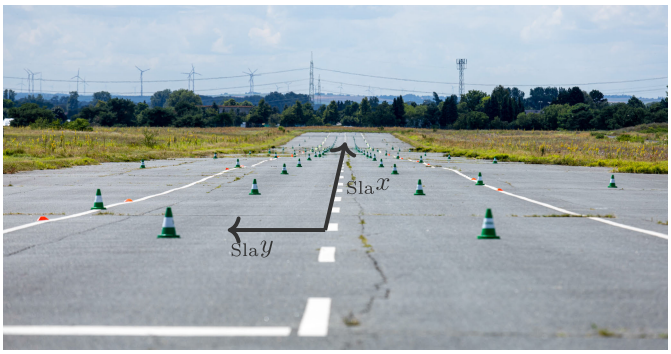

Fig. 4. Slalom course marked with traffic cones and slalom-centered coordinate system.

in a constant function with the same value as the amplitude of the slalom. However, due to human errors and environmental impacts, $z(x)$ oscillates unevenly along x_{OOI}. In the next step, this function can be easily described by its mean value $\overline{|z(x)|}$ and the according to variance $s^2(z(x))$, which is referred to as s^2 henceforth. To consider deviation from the ideal mean value and the variance, the final unitless quality criterion is calculated as shown in the following equation with the optimal value of 2:

$$k_{\mathrm{Q}} = \begin{cases} \dfrac{s^2_{\max} - s^2}{s^2_{\max} - s^2_{\mathrm{id}}} + \dfrac{\overline{|z(x)|} - \overline{|z(x)|}_{\min}}{\overline{|z(x)|}_{\mathrm{id}} - \overline{|z(x)|}_{\min}}, & \overline{|z(x)|} \leq 5\ \mathrm{m} \\ \dfrac{s^2_{\max} - s^2}{s^2_{\max} - s^2_{\mathrm{id}}} + \dfrac{\overline{|z(x)|}_{\max} - \overline{|z(x)|}}{\overline{|z(x)|}_{\max} - \overline{|z(x)|}_{\mathrm{id}}}, & \overline{|z(x)|} > 5\ \mathrm{m}. \end{cases} \tag{3}$$

Here, $s^2_{\max}$ is set as 0.05 m^2 which represents a subjectively chosen threshold based on the rough evaluation of previous test runs. Likewise, the thresholds for the mean value are defined as $\overline{|z(x)|}_{\max} = 5.2$ m and $\overline{|z(x)|}_{\min} = 4.8$ m. Furthermore, the ideal values are defined as $s^2_{\mathrm{id}} = 0$ and $\overline{|z(x)|}_{\mathrm{id}} = 5$ m, which reflect the ideal sinusoidal trajectory with an amplitude of 5 m. The quality criterion is normalized in a way that each summand equals 1 when the mean value, respectively, the variance, equals the ideal value. As soon as one of the two variables passes the minimum/maximum threshold value, the corresponding summand becomes negative. In conclusion, the ideal trajectory results in $k_{\mathrm{Q}} = 2$ and decreases steadily with increasing variance s^2 and increasing absolute difference $|\overline{|z(x)|} - 5|$.

Out of the test runs of each vehicle, the runs of the highest quality can be determined by calculating the corresponding quality criteria. These runs are of the highest available reproducibility. Fig. 5 shows the achieved precision of the driver's trajectory during all test runs. The red dashed lines represent the predefined threshold values for the mean value and the variance. On average, the achieved mean value lies below the ideal of 5 m. This is most likely due to the fact that the driver orients himself to the traffic cones on the inner side of each vertex. Factors influencing the variance include different vehicles, human factors, for example, seating positions as well as fatigue and driver experience in handling various vehicles.

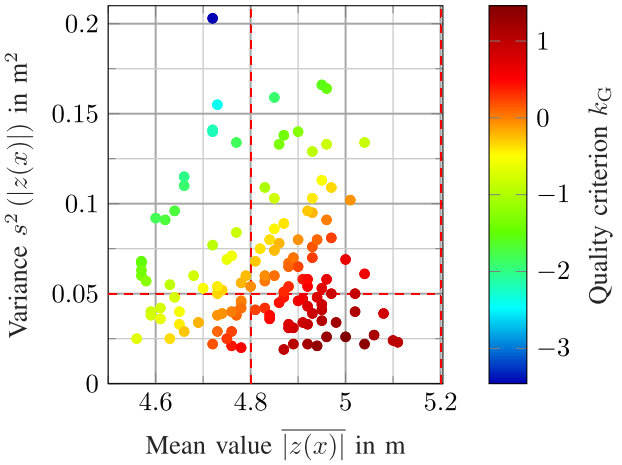

Fig. 5. Achieved precision of driver trajectory, quantified by the mean value of the Hilbert transformation's absolute, and the corresponding variance. The red dashed lines indicate the predefined thresholds for mean value and variance.

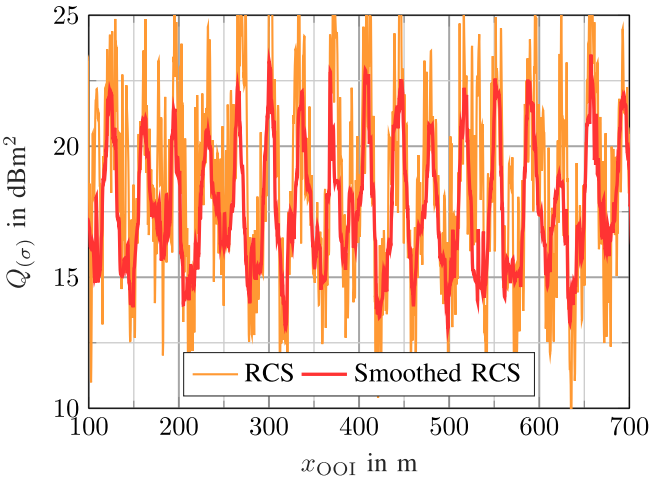

Fig. 6. RCS of Toyota Auris observed while it is driving through the slalom. A periodic pattern is visible after moving median smoothing.

III. Results

Core results, that are available from our measurement campaign, are outlined in this section and are structured according to the research questions in Section I-B. Each plot can be generated for different vehicles and sensors with the MATLAB tool that is released alongside this article. We show detailed measurement results for a Toyota Auris, representing a medium-size vehicle, and extend our findings to the full vehicle dataset.

A. Influence of Aspect Angle

We begin with a typical result of the RCS profile obtained during one slalom run. It is shown in Fig. 6 and reveals a periodical pattern, which is more distinct after smoothing with a moving median filter. In the smoothed signal, we can obtain a mean RCS value of approximately 18 dBm^2 with peak amplitudes of approximately 4 dBm^2. In the raw signal, the RCS shows sporadic peaks that span between 13 and 25 dBm^2. Qualitatively similar patterns can be found for all vehicles by executing the "RCS over x" plot in the MATLAB program.

Fig. 7 shows the RCS again, but now plotted over azimuth and yaw angle. Slalom driving renders as circles in this

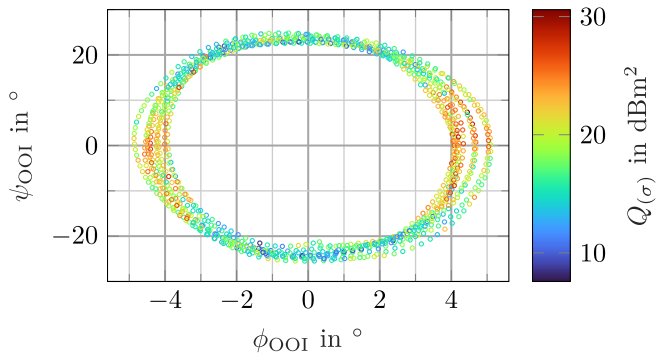

Fig. 7. RCS profile of Toyota Auris over azimuth ϕ_{OOI} and yaw ψ_{OOI}.

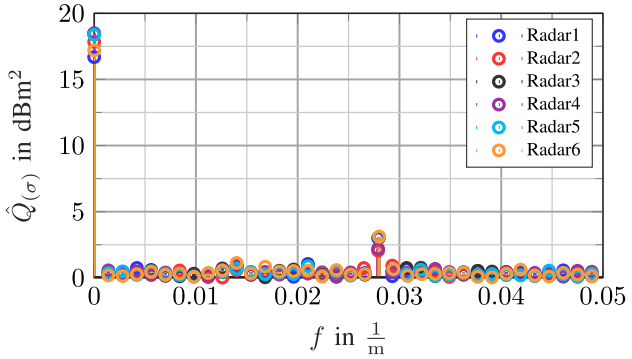

Fig. 8. Spectral analysis of RCS during the same slalom. $\hat{Q}_{(\sigma)}$ denotes the amplitude of the oscillating RCS pattern. Only minor differences in measurements between sensors at the dc-component (zero-frequency) and double harmonic frequency are visible.

representation. The RCS trends to its maximal value at close to zero yaw, that is, at maximal azimuth and minor mitigation is visible through the trial. The minimal values are found at zero azimuth but maximum yaw, that is, as the OOI is crossing through the boresight line during driving through the slalom. From both figures, we can conduct a major influence of the yaw angle on the RCS profile. This plot is generated with the "RCS over yaw and azimuth" function in the MATLAB program.

B. Influence of Mounting Height

To reveal governing frequencies visible in the harmonic course, we obtain a spectral analysis of the signal via fast Fourier transform (FFT) on the RCS over range, which was shown in Fig. 6. A typical result is shown in Fig. 8, which shows the single-sided amplitude spectrum over all radar sensors. This plot is generated with the "FFT over x" plotting function in the MATLAB program. The FFT reveals the signal amplitudes at the dominant frequencies in the signal. At zero frequency, the FFT gives the dc component, which is the amplitude at zero frequency, as the quasi-mean value of the periodic RCS signal. It shows an additional peak at double the natural frequency of the slalom, which is around 0.028(1/m). This is due to the orientation and therefore visibility of the OOIs' left- and right-hand sides. The changes in the respective magnitudes indicate the effect of the sensor mounting height and vehicle body shapes. Noise components will render minor spectral components outside these two frequencies.

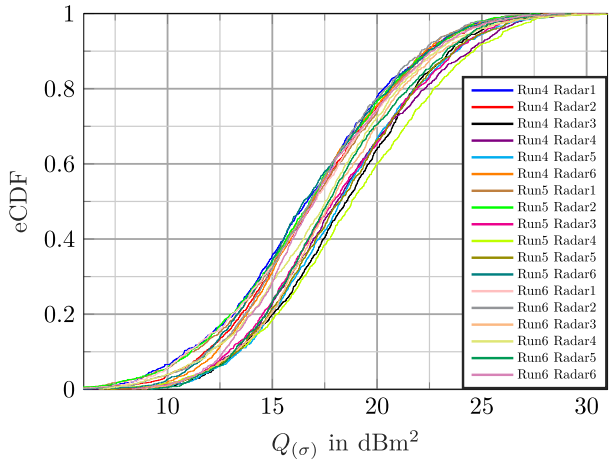

Fig. 9. eCDF plot of Toyota Auris' RCS of all six radar sensors and the three best runs in terms of the Hilbert criteria.

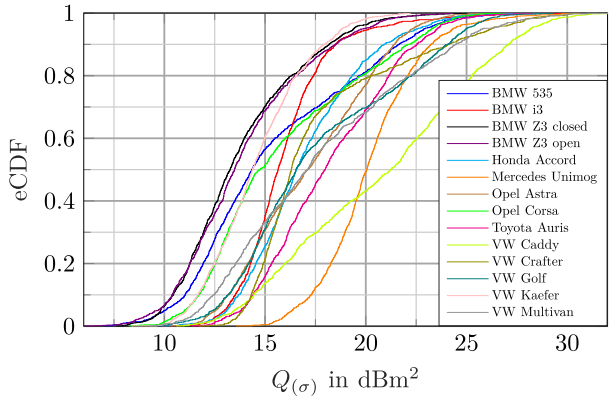

Fig. 10. eCDF plot of all OOI's summed RCS of all radar sensors of the best run in terms of the Hilbert criterion.

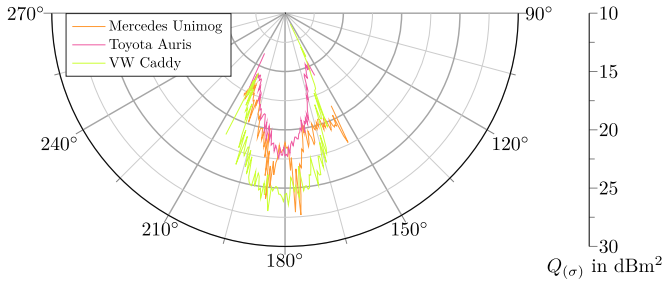

Fig. 11. RCS profiles of Mercedes-Benz Unimog, Toyota Auris, and VW Caddy.

We can only notice a little spread in RCS between sensors, which is below 3 dBm^2 and therefore small compared to its total dynamic range. It is to emphasize that these amplitudes do not represent an absolute RCS value, but the amplitudes of the oscillation of RCS during the slalom. The relation of the amplitude at the harmonic frequency to the amplitude at 0 quantifies its dynamic range. The difference between the two amplitude levels can be understood as the sensitivity of a particular vehicle body to the aspect angle. The higher the amplitude at the harmonic frequency, the higher the range between minimal and maximal observed RCS during the slalom.

So far, we have only discussed the amplitudes obtained by the FFT-based spectral analysis. The RCS measurements are characterized by considerable noise, which leads to significant

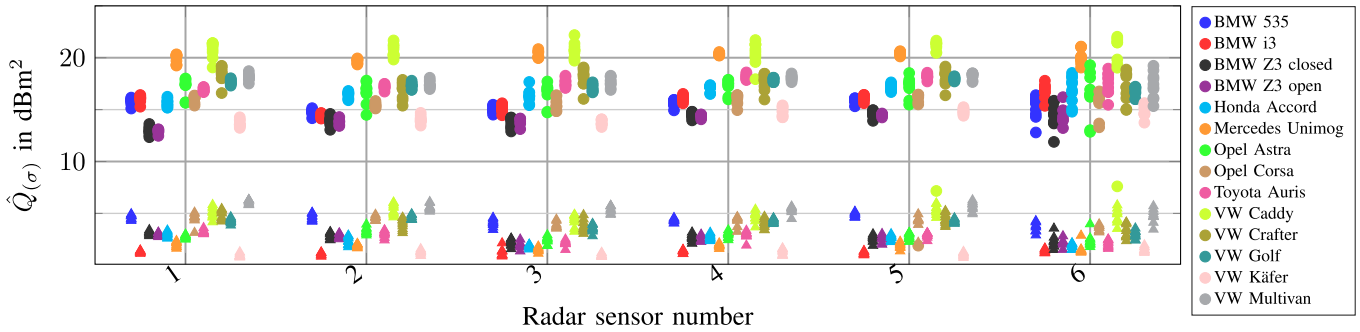

Fig. 12. Spread of spectral amplitudes obtained by FFT over all studied cars and trials. Circles denote zero-frequency amplitude, and triangles indicate amplitude at the double natural frequency. The figure shows all radar sensors and vehicles simultaneously for the best comparison.

outliers with particularly high or low RCS values. To analyze the quantitative distribution, we compute the eCDF, showing the distribution of samples and the frequency of their occurrence. Fig. 9 visualizes the eCDF of the six radar sensors and three best runs regarding the Hilbert criterion of the Toyota Auris. In general, all graphs show almost identical behavior and are lying within a 2-dBm^2 range. From this finding, we conclude that the previously mentioned noise is present in a similar manner in all six radar sensors as well as in all runs. An explanation for the recognizable spread beside the stochastic character of the RCS is the run quality, but also different distances between the Ego and the OOI. The distribution of the RCS is another indication that the influence of the sensor mounting height on the reflectivity characteristics of vehicles is lost in the signal bandwidth of the RCS itself.

C. Influence of Body Shape

For studying the behavior of different vehicle bodies, the spectral FFT analysis is now extended to the full set of vehicles and sensors. Therefore, their spread during multiple test repetitions becomes quantitatively specifiable. This gives objective insights into how well the repeatability of the experiment, that is, how well similar results can be obtained in a repeated trial.

We focus on the amplitudes at the dc component and the doubled natural frequency. Fig. 12 shows the spectral amplitudes obtained by FFT over all studied cars, trials, and mounting heights. The preliminary finding from the Toyota Auris, as presented above, can be well transferred to the other vehicles. While each vehicle differs in amplitude, we see a little spread across sensors and repetitions. Differences between vehicle bodies become more notable when taking the amplitudes at the doubled natural frequency into account. Here, we see that large amplitudes at the dc component are not necessarily followed by large amplitudes at the double natural frequency. Of particular note are the Mercedes-Benz Unimog and the BMW i3, which show strong dc component amplitudes, but only minor amplitudes at the doubled natural frequency. Contradicting examples are given by the VW Multivan and VW Caddy. From this result, we further justify minor influences of the sensor mounting position, which is less than 3 dBm^2 across all studied vehicles. The highest spread is present at radar sensor 6, which is closest to the ground. At the same time, variations between multiple trials remain at the same level.

To view the RCS distributions in addition to the FFT spectral analysis, the eCDF graphs of the different vehicles are visualized in Fig. 10. The eCDFs shows significant differences between all vehicles. No direct correlation between vehicle size and RCS can be seen. This can be especially demonstrated by comparing Honda Accord or VW Multivan and Toyota Auris. Furthermore, the eCDF of the Mercedes-Benz Unimog resembles a log-normal distribution despite its complex structures on the sides. This is also evident for BMW i3, Honda Accord, Opel Astra, Toyota Auris, and VW Käfer. BMW 535, BMW Z3, Opel Corsa, VW Caddy, VW Crafter, VW Golf, and VW Multivan exhibit a kind of kink in the distribution function, which resembles a log-logistic distribution. Therefore, not only the quantitative value of RCS differs, but also the distributions are different between all vehicles. No direct correlation between body size, shape, and material can be identified. Therefore, other radar sensors and mounting positions are the focus of future work.

The FFT analysis and the eCDF do not give information about the noise and sensitivity of the RCS at individual yaw angles. To take these aspects into account, it is recommended to display the RCS in a polar plot. From the findings in Fig. 9, we conclude that on the basis of the Hilbert criterion, an evaluation of the trajectories regarding their comparability is reasonable. Therefore, the different radar sensors as well as the three best runs of the vehicles are aggregated. The summed RCS values from each time step are assigned to the yaw angle ${}_S\psi_{OOI}$, which is discretized with 0.5°. Subsequently, the median of the RCS is formed for each discrete yaw angle and displayed in a polar plot. Fig. 11 shows RCS profile for all radar sensors and the three best runs for the Unimog, the Auris, and the Caddy. Toyota Auris and VW Caddy show a qualitatively similar RCS character, with the VW showing a significantly higher as well as more brawny shaped pattern. The many add-on parts and the complex structures of the Unimog result in an asymmetrical RCS profile, which is clearly distinguishable from all other vehicles.

Due to the fact that based on the experimental setup, the projected area of the vehicle at ${}_S\phi_{OOI} \neq 0$ is higher in comparison to a turntable in an anechoic chamber the RCS profile differs from a laboratory profile. Nevertheless, the measured characteristics of the vehicles can be used for validation purposes in sensor simulation.

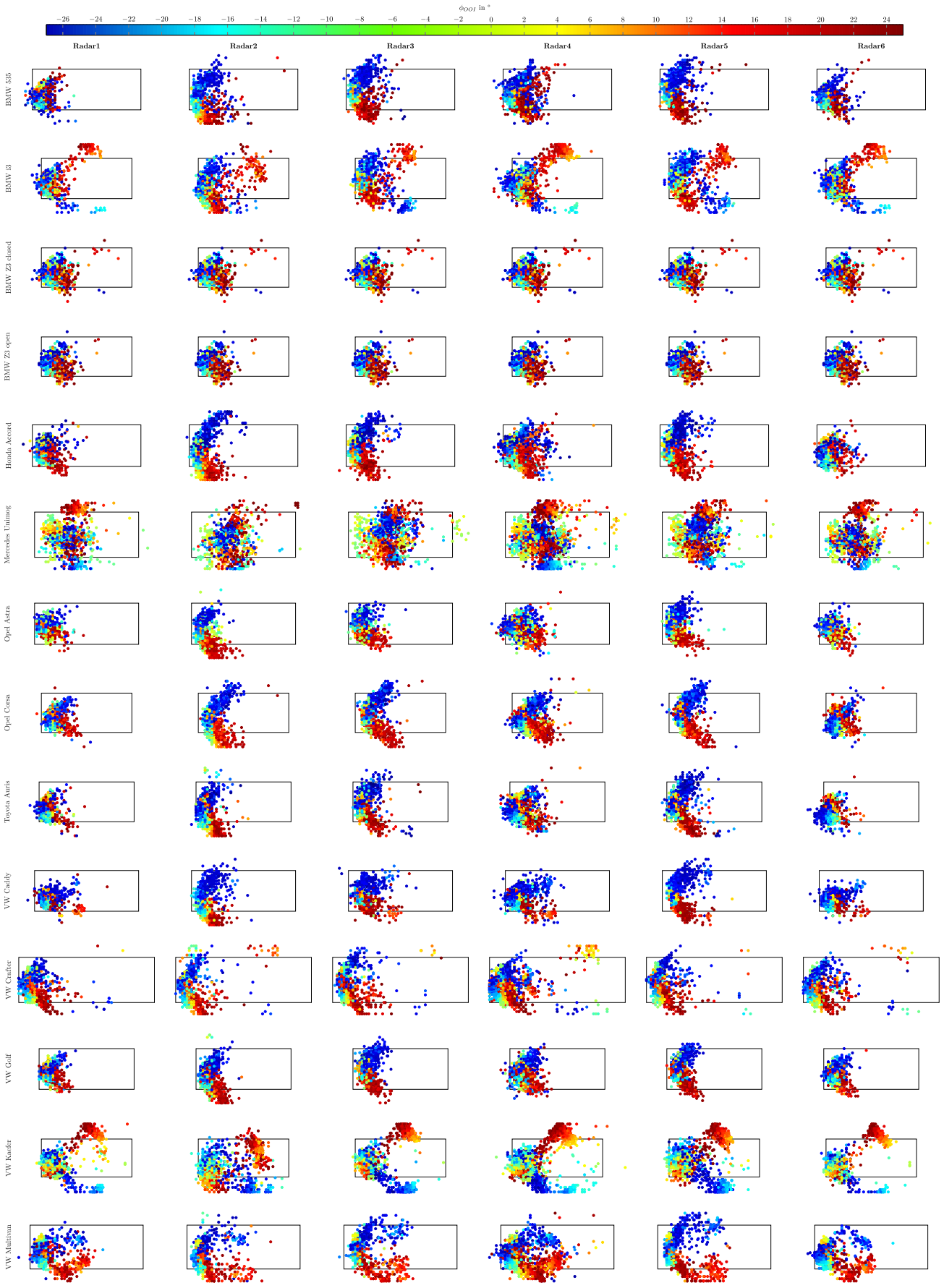

Fig. 13. Location of detections with the highest RCS per measurement cycle around and inside the bounding box for each vehicle and each radar sensor. For evaluation, we took the best run in terms of the Hilbert criterion.

D. Strongest Scatter Location

For a deeper analysis, we consider the distribution of the detections with the highest RCS over the bounding box of the different vehicles. Fig. 13 shows the detection location of the best run of each vehicle and each radar sensor. Therefore, only the detection with the highest RCS is visualized to gain insights into the main scattering parts of each vehicle. The yaw angle difference ${}_S\psi_{OOI}$ between Ego and OOI is coded as color identifier. Additionally, the bounding boxes of the different vehicles are represented in the form of black rectangles. The detections outside of the bounding box can be explained by timing effects due to different measurement frequencies as well as the resolution of the radar sensor itself. In general, the detections are at the rear center of the vehicles, as already shown in [9]. Slight differences between radar 1/6 and radar 2/3/4/5 are visible for BMW 535, Honda Accord, Opel Corsa, Toyota Auris, and VW Caddy. Special features in the distribution can be seen in the BMW i3, which is equipped with a carbon body, the Unimog, which has various add-on parts at the rear and side, the Crafter, which shows detections on the wheel arches at the front, and the Käfer, which has CCR-shaped side sills. Therefore, we conclude that the position distribution of the detections depends on the body shape as well as on the yaw angle between the sensor and OOI.

IV. Derived Findings for Sensor Simulation

We summarize the core results of our research from various points of view as follows. Here, we focus on statements that are of immediate value to the sensor simulation research community.

A. Analytical RCS Models

Sensor modeling must take into account the fact that even a reference measurement can never be made with infinite accuracy. Uncertainties remain, which are difficult to quantify but remain visible as nondeterministic and stochastic behavior. This becomes particularly clear in the deviations of the RCS measurements between the tests. Our results stress the stochastic nature of the RCS characteristics of vehicles. For each vehicle geometry, we find differences at the microscopic level that justify deviations in the RCS. Due to a large number of possible geometries of today's and future cars, we consider it difficult to maintain vehicle-specific analytical RCS models. In object-based sensor modeling, a generative model can be derived from our data that returns an RCS value for a given aspect angle. For other modeling approaches, our work gives reference measurements that can be used for simulation model falsification.

B. Spatial Distribution of Detections

We identified clear differences in the spatial distribution of detections around the vehicles. The Volkswagen Käfer is of particular note: Its body design at the bottom of the front door forms a CCR-shape and leads to a concentration of detections around this area.

These results, however, pose a challenge for traditional scattering center models. They assume "fixed" areas of significant scatter, while our results show that these areas differ significantly between vehicle shapes [6]. This also poses a challenge for object detection algorithms, relying on detection clustering. The centerpoint of clusters varies between vehicles, resulting in a systematic position offset between the true and estimated position of the vehicle.

C. Sensor Model Validation

Our results and dataset can serve as a baseline for sensor model validation. The RCS behavior obtained during reenacting the slalom drive in the virtual world should match its eCDF distribution. In "physical," or "reflection-based" sensor simulation, the detailing of 3-D models is of high importance. These models must convey material descriptions and meshing must be fine enough to preserve geometrical details. By comparing the spatial distribution of the detections, the appropriateness of 3-D models for radar simulation becomes judgeable.

Sensor models that process object information as input data do benefit from our work by having access to a publicly available dataset that allows model parameterization.

D. Transferring Results to Other Radar Sensors

The gathered RCS data and detection distribution are only valid for Continental ARS408 sensors. However, when gathering the same data with other radar sensors, the RCS profiles presented in Fig. 11 are expected to look similar in their qualitative form and the stochastic RCS behavior will have a similar dynamic range. It is also expected that the detection focal point of the spatial distribution will be identical for the various vehicles. By using radar sensors with higher resolutions, the position of the (strongest) detection can be determined more precisely. Still, our results are well aligned with previous research, such as [9], which utilizes the SAR method. In future research, radar sensors with elevation measurements are expected to lead to further insights into the 3-D location of detections.

V. Conclusion

The aim of the work was to investigate the aspect angle dependence of the RCS. For this purpose, an experimental setup was proposed in which the vehicle under investigation drives a slalom while being observed by several radar sensors.

The design of our slalom aims at minimizing uncertainties in radar perception introduced by human drivers. Hereby, we could isolate the noise that is typically present in radar measurements to the radar measurement principle. At the same time, additional influences, such as unsteady driving through a slalom course by human drivers, are isolated.

From the measurement results, we gained knowledge about the stochastic behavior of the RCS and the local distribution of the detections.

For further work, we recommend examining the SNR value in addition to the RCS value. While this will show proportionality to the RCS value, it has the advantage of taking into account the performance of the radar. Thus, the SNR value

is easier to determine than the RCS because, for example, the antenna pattern and frequency filters have no influence. When setting up the test again, we recommend considering an additional radar, which is installed with a horizontal offset. This can be used to draw conclusions about the transferability between horizontal shoring positions. In our work, we have shown that the vertical shoring position has a negligible part. The evaluation methodology can be applied straightforwardly to lidar sensors as well. In this way, similar investigations of reflectivity can also be performed for lidar sensors.

Furthermore, by providing ground truth and vehicle metadata, our dataset also provides a scientific basis for defining detection-level metrics of sensor data. This is the subject of ongoing research for the evaluation of sensors and simulations and also in the interest of industrial standardization processes.

ACKNOWLEDGMENT

The authors would like to thank the owners of the used vehicles for making them available for this study. They also gratefully acknowledge Prof. Hermann Winner for his guidance and advice, and Prof. Steven Peters, Clemens Linnhoff, and Philipp Rosenberger for proofreading.

REFERENCES

[1] R. B. Dybdal, "Radar cross section measurements," *Proc. IEEE*, vol. 75, no. 4, pp. 498–516, Apr. 1987.

[2] H. Winner, "Automotive RADAR," in *Handbook of Driver Assistance Systems*. Cham, Switzerland: Springer, Dec. 2015, pp. 325–403, doi: 10.1007/978-3-319-12352-3_17.

[3] K. Werber et al., "Automotive radar gridmap representations," in *IEEE MTT-S Int. Microw. Symp. Dig.*, Apr. 2015, pp. 1–4.

[4] K. Karlsson, H. Toss, J. Lang, F. Costagliola, T. Zheng, and E. Marel, "Hifi radar target: High fidelity soft targets and radar simulation for more efficient testing (real and virtual)," Res. Inst. Sweden (RISE), Saf. Transp., Electron., Tech. Rep., 2019. [Online]. Available: http://www.diva-portal.org/smash/record.jsf?pid=diva2%3A1264147&dswid=-5305

[5] E. B. Kamel, A. Peden, and P. Pajusco, "RCS modeling and measurements for automotive radar applications in the W band," in *Proc. 11th Eur. Conf. Antennas Propag. (EUCAP)*, Mar. 2017, pp. 2445–2449.

[6] P. Swerling, "Probability of detection for fluctuating targets," *IRE Trans. Inf. Theory*, vol. 6, no. 2, pp. 269–308, Apr. 1960, doi: 10.1109/tit.1960.1057561.

[7] S. B. J. Gowdu, A. Schwind, R. Stephan, and M. A. Hein, "Monostatic RCS measurements of a passenger car mock-up at 77 GHz frequency in virtual environment," in *Proc. 49th Eur. Microw. Conf. (EuMC)*, Oct. 2019, pp. 996–999. [Online]. Available: https://ieeexplore.ieee.org/document/8904569

[8] I. Matsunami, R. Nakamura, and A. Kajiwara, "RCS measurements for vehicles and pedestrian at 26 and 79GHz," in *Proc. 6th Int. Conf. Signal Process. Commun. Syst.*, Dec. 2012, pp. 1–4, doi: 10.1109/icspcs.2012.6508004.

[9] M. Andres, P. Feil, and W. Menzel, "3D-scattering center detection of automotive targets using 77 GHz UWB radar sensors," in *Proc. 6th Eur. Conf. Antennas Propag. (EUCAP)*, Mar. 2012, pp. 3692–3693, doi: 10.1109/eucap.2012.6206580.

[10] S. Abadpour, A. Diewald, M. Pauli, and T. Zwick, "Extraction of scattering centers using a 77 GHz FMCW radar," in *Proc. 12th German Microw. Conf. (GeMiC)*, Mar. 2019, pp. 79–82, doi: 10.23919/gemic.2019.8698144.

[11] A. Palffy, E. Pool, S. Baratam, J. F. P. Kooij, and D. M. Gavrila, "Multi-class road user detection with 3+1D radar in the view-of-delft dataset," *IEEE Robot. Autom. Lett.*, vol. 7, no. 2, pp. 4961–4968, Apr. 2022.

[12] O. Schumann et al., "RadarScenes: A real-world radar point cloud data set for automotive applications," in *Proc. IEEE 24th Int. Conf. Inf. Fusion (FUSION)*, Nov. 2021, pp. 1–8, doi: 10.23919/fusion49465.2021.9627037.

[13] H. Caesar et al., "NuScenes: A multimodal dataset for autonomous driving," in *Proc. IEEE/CVF Conf. Comput. Vis. Pattern Recognit. (CVPR)*, Jun. 2020, pp. 11621–11631.

[14] M. F. Holder, "Synthetic generation of radar sensor data for virtual validation of autonomous driving," Ph.D. dissertation, Inst. Automot. Eng. Darmstadt, Technische Universität Darmstadt, Darmstadt, Germany, 2021. [Online]. Available: http://tuprints.ulb.tu-darmstadt.de/17545/

[15] C. E. Services. *Data Sheet Continental ARS 408-21 Premium Long Range Radar Sensor 77 GHz*. Accessed: Jan. 13, 2023. [Online]. Available: https://www.continental-automotive.com/getattachment/8e4678e1-9358-48e1-8d5b-a0c2de942edb/ARS408-21_Datenblatt_de_170707_V07.pdf.pdf

[16] Mercedes-Benz. *GLS SUV Specification*. Accessed: Sep. 27, 2022. [Online]. Available: https://www.mercedes-benz.co.za/passengercars/mercedes-benz-cars/models/gls/suv-x167/specifications/dimensions/_jcr_content/highlightcontainer/par/highlighttile_1222582405.MQ6.0.2x.20190627112735.jpeg

[17] *Richtlinien Für die Anlage von Landstraßen*, Forschungsgesellschaft Für Straßen und Verkehrswesen e.V., Bonn, Germany, 2012. [Online]. Available: https://www.fgsv-verlag.de/pub/media/pdf/201.r.16052013.pdf

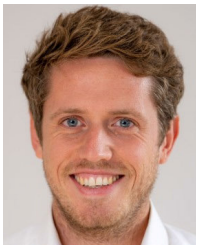

Lukas Elster was born in Fulda, Germany, in 1993. He received the B.Sc. and M.Sc. degrees in mechanical engineering from TU Darmstadt, Darmstadt, Germany, in 2016 and 2020, respectively.

Since 2020, he has been working as a Research Associate with the Institute of Automotive Engineering, TU Darmstadt. His research interests include the effects of radar and lidar sensors in complex surroundings.

Martin F. Holder was born in Heilbronn, Germany, in 1990. He received the Dr.-Ing. degree in radar sensor simulation from TU Darmstadt, Darmstadt, Germany, in 2021, the master's degree in mechanical engineering from TU Darmstadt, in 2016, and the master's degree in systems, control and mechatronics from Chalmers University, Gothenburg, Sweden.

Manuel Rapp was born in Saarbrücken, Germany, in 2000. He received the B.Sc. degree in mechanical engineering from TU Darmstadt, Darmstadt, Germany, in 2021.

Since then, he has been working as a Research Assistant with the Institute of Automotive Engineering, TU Darmstadt.